Kenzo Sasaki · Gilles Tissot · André V. G. Cavalieri · Flávio J. Silvestre · Peter Jordan · Damien Biau

Closed-loop control of a free shear flow: a framework using the parabolized stability equations

Abstract In this study the parabolized stability equations (PSE) are used to build reduced-order-models (ROMs) given in terms of frequency and time-domain transfer functions (TFs) for application in closed-loop control. The control law is defined in two steps; first it is necessary to estimate the open-loop behaviour of the system from measurements, and subsequently the response of the flow to an actuation signal is determined. The theoretically derived PSE TFs are used to account for both of these effects. Besides its capability to derive simplified models of the flow dynamics, we explore the use of the TFs to provide an a priori determination of adequate positions for efficiently forcing along the direction transverse to the mean flow. The PSE TFs are also used to account for the relative position between sensors and actuators which defines two schemes, feedback and feedforward, the former presenting a lower effectiveness. Differences are understood in terms of the evaluation of the causality of the resulting gain, which is made without the need to perform computationally demanding simulations for each configuration. The ROMs are applied to a direct numerical simulation of a convectively unstable 2D mixing layer. The derived feedforward control law is shown to lead to a reduction in the mean square values of the objective fluctuation of more than one order of magnitude, at the output position, in the nonlinear simulation, which is accompanied by a significant delay in the vortex pairing and roll-up. A

Communicated by Daniel J. Bodony.

K. Sasaki (✉) · G. Tissot · A. V. G. Cavalieri · F. J. Silvestre
Instituto Tecnológico de Aeronáutica, São José dos Campos, Brazil
E-mail: kenzo@ita.br

G. Tissot
E-mail: tissot.gilles@gmail.com

A. V. G. Cavalieri
E-mail: andre@ita.br

F. J. Silvestre
E-mail: flaviojs@ita.br

G. Tissot
Present address: Institut de Mathématiques de Toulouse, Universit Paul Sabatier, Toulouse, France

P. Jordan
Institut Pprime, Poitiers, France
E-mail: peter.jordan@univ-poitiers.fr

D. Biau
DynFluid Laboratory, Arts et Métiers ParisTech, Paris, France
E-mail: damien.biau@ensam.eu

study of the robustness of the control law demonstrates that it is fairly insensitive to the amplitude of inflow perturbations and model uncertainties given in terms of Reynolds number variations.

Keywords Closed-loop flow control · Reduced-order-modelling · Inversion controllers · Instability control

1 Introduction

The manipulation of flow dynamics through active or passive control strategies represents a challenge with several industrial and technological applications. Reduction in drag and consequently of fuel consumption, delay in the transition to turbulence of laminar flows, and reduction in noise levels are but a few of the foreseeable applications of flow control [29].

Over the last years, passive and active flow manipulation has been accomplished. Passive control has been achieved, for boundary layers, via the introduction of roughness elements, as in the work of [49] or by means of chevrons in turbulent jets which attenuate large scale structures [8,31]. For the active, open-loop case, Biringen [7] used suction and blowing in order to obtain the delay in transition in a channel flow. Koenig et al. [30] and Le Rallic et al. [32] use the continuous injection of air in the core of a turbulent jet in order to diminish the radiated acoustic emission. Active closed-loop control is also possible, as the initial stages of the transition of laminar shear flows is a linear process [28], and there are numerous examples of such in the literature, which will be presented in greater depth during this section.

There are still, however, obstacles that prevent the use of active closed-loop control in most practical applications. The main difficulty relates to the fact that the Navier–Stokes equations, which determine the dynamics of a flow, are nonlinear and therefore require a simplification in order to allow the use of linear control theory. Added to this is the fact that fluidic problems normally present a high-dimensionality. From a flow control point of view, each flow variable at each grid point of the discretized system may be treated as a degree of freedom, making the computational requirements, not only of the simulated system, but also of the online actuation computation, grow rapidly with the domain of calculation.

Such computational difficulties mean that it is not feasible to design full-order compensators or to deal with the full system [42], and a common approach is to start by reducing the order of the problem, and designing the gains using the reduced-order system—such a strategy is usually referred to as reduce-then-design. The assessment of the closed-loop stability and performance is then made a posteriori in the full nonlinear simulation.

The reduce-then-design idea has been successfully applied in numerous works. The problem lies in finding, starting from the linearized Navier–Stokes system, linear reduced-order models that allow determination of the relationship between the defined inputs (external disturbances and actuators) and outputs (flow quantities measured by a finite number of sensors) of the system. Once such model is available, several techniques are applicable: optimal linear quadric regulators, robust controllers, among others. An introductory review to such techniques is presented in the works of Bagheri et al. [3] and Kim and Bewley [29].

In the works of Fabbiane et al. [16–18], an identification technique, denoted eigensystem-realization algorithm (ERA) [27] is used to construct reduced-order models that reproduce the impulse responses computed from a linearized Navier–Stokes simulation. Feedforward optimal compensators both for two- and three-dimensional boundary layers are then built from the ERA state-space model. The models so obtained have about a hundred degrees of freedom. A drawback of ERA is that the linear system so obtained has state variables that cannot be related to flow quantities such as velocity and pressure.

It is also possible to proceed in an entirely empirical way, using system identification to determine a model for the aforementioned relationship between inputs and outputs. Examples of such are available in the works of Gautier and Aider [19] and Hervé et al. [22], both of which rely on ARMAX (Auto-Regressive-Moving-Average-eXogenous) [1] models and also deal with a feedforward control law. ARMAX leads to a time-domain single-input-single-output model built from previously obtained unsteady measurements. The determination of the number of required coefficients is also required, adding a higher degree of empiricism to the model.

These different approaches have a compelling performance in capturing the behaviour of the time-domain fluctuations, but have the drawback of requiring a learning dataset, being dependent of the configuration of sensors and actuators. A simulation or experiment has to be performed a priori, with fixed sensors and actuators, which will supply the data for the construction of the reduced-order models. If the choice of sensors and actuators is modified, a new simulation is required, since the model reduction is performed only after such choice of inputs and outputs of the system. Hence, optimization of sensors and actuators can become a

cumbersome task, since each choice requires a new reduced-order model. This is of particular interest when one considers the energy budget for actuation; in the work of Fabbiane et al. [16] it is shown that the currently available actuators for flow control applications for transition delay are close to the break-even point. An a priori determination of the optimal actuator/sensor positions could increase the efficiency of such controllers.

In this work, we propose an alternative strategy, using a reduced-order model based on the physics of the convectively unstable flow that we consider, acting via a destructive interference of the incoming wavepacket. Initial works dealing with this type of actuation could be tracked down to some of the first flow control implementations, such as the works of Thomas and Saric [45] and Thomas [46].

The works cited above dealt with single-frequency disturbances. The work of Li and Gaster [35] improves on such ideas by dealing with broadband perturbations by means of transfer functions, formulated using linear stability theory to predict the spatial and temporal behaviour of Tollmien–Schlichting waves in a flat plate. The control law is then able to delay the transition to turbulence in an experimental implementation.

We continue to build up on these ideas by improving the fidelity of the ROM by using parabolized stability equations (PSE) [21], which account for the slow divergence of the baseflow. This follows our previous efforts in Sasaki et al. [40] on which similar strategies are applied to a turbulent jet.

The added advantage that is explored is the possibility of using the ROM to rapidly explore the positions to be used as input and outputs: This can be done from a single PSE solution encompassing the range of relevant frequencies, since model reduction is performed independently of sensor and actuator placement. The framework for the choice of control positions is then posed by evaluating the sensitivity of the flow to actuation, the causality of transfer functions and the effectiveness of models. The control law we propose is the direct inversion of the system, which we obtain in the frequency domain and leads, in the time domain, to a wave-cancelling signal at the objective position.

The ROMs and control techniques are applied to a two-dimensional mixing layer, computed by a direct numerical simulation (DNS). Mixing layers are a canonical problem for the study of sound generation by low-Reynolds free shear flows [9,12,48]. With the present incompressible simulation, it is not possible to compute directly the sound radiation. However, it allows an evaluation of the capability of the controller in suppressing or delaying vortex roll-up and pairing, which in turn is expected to lead to reduction in the radiated sound of the analogous, compressible scenario.

The paper is organized as follows. In Sect. 2 a brief description of the flow and nonlinear numerical simulation is introduced. In Sect. 3 the reduced-order models used for the estimation and actuation are introduced. In Sect. 4 the control laws are introduced, a baseline case, using the feedforward scheme is presented in 5 both in the linear and in the nonlinear cases. An evaluation of the robustness of the controller is presented in Sect. 5. The effects of placement of the actuator along the transverse direction and its relative position to the input are evaluated in Sects. 7 and 8, respectively. Concluding remarks are drawn in Sect. 9. A brief description regarding the parabolized stability equations and the Kelvin–Helmholtz projection are included in "Appendix".

2 2D nonlinear numerical simulation

The numerical simulation of the two-dimensional Navier–Stokes equations is used to test the transfer functions for the estimation and control, along with the designed control schemes.

The two-dimensional Navier–Stokes equations are solved with a Chebyshev spectral collocation method in the transverse direction (Y) and Fourier decomposition in the streamwise direction (X). The Gauss–Lobatto–Chebyshev grid is expanded from the interval $[-1,\ 1]$ to the physical domain $[-Y_\infty, Y_\infty]$ through an algebraic mapping. The time-marching combines a fourth-order Adams–Bashforth scheme and a fourth-order backward differentiation scheme, with viscous term treated implicitly [6]. The domain is $X = [0 : L_X], Y = [-Y_{\text{inf}} : Y_{\text{inf}}]$ with $L_X = 600$ and $Y_{\text{inf}} = 200$, discretized with $N_X = 512$ and $N_Y = 70$.

The simulation non-dimensional time step is $\Delta t = 0.02$, where solutions are stored every $\Delta t_{\text{save}} = 0.4$ for a time $T = 2000$, where the non-dimensionalization is defined with respect to a reference velocity ΔU, equal to the difference in velocity across the shear, and the vorticity thickness δ_w given by,

$$\delta_w = \frac{\Delta U}{\max\left(\partial u/\partial y\right)|_{x=0}} \tag{1}$$

The inflow condition is specified as

$$U_b(Y) = \frac{1}{2}\left(1 + \tanh\left(\frac{Y}{2}\right)\right), \tag{2}$$

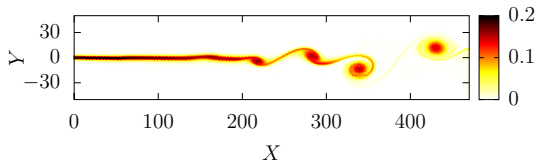

Fig. 1 Instantaneous vorticity field of the mixing layer DNS

plus unsteady perturbations given as low-pass filtered white noise at the inflow. The resulting maximum RMS root-mean-squared values at the inflow is of 10^{-4}, and these disturbances are amplified by the Kelvin–Helmholtz instability and generate vortex roll-up and pairing that is non-periodic, leading to a broadbanded disturbance spectrum in the DNS. Figure 1 shows a typical flow snapshot.

The inflow (2) imposes a unitary velocity difference across the shear ΔU and a unitary vorticity and momentum thickness. The Reynolds number used is based on the vorticity thickness and the velocity difference, $Re = \frac{\Delta U \delta_\omega}{\nu} = 100$, where ν is the kinematic viscosity. In what follows, the X- and Y-components of velocity are denoted as $u(t)$ and $v(t)$, and pressure as p. Non-dimensional frequencies are presented as a Strouhal number $St = f\delta_\omega/\Delta U$, where f is the frequency.

Because we are using a Fourier decomposition in the non-homogeneous streamwise direction, a sponge zone is applied at the end of the domain, so that the solution $q_\phi = (u, v, p)^{\mathrm{T}}$ reaches the inflow state q_{in}. It consists of adding a forcing term $\mathbf{f} = -\lambda(\mathbf{q}_\phi - \mathbf{q}_{\mathrm{in}})$ with $\lambda = \frac{20}{2}\left(1 + \tanh\left(\frac{X - 0.85\,L_X}{10}\right)\right)$.

3 Reduced-order modelling

3.1 Estimation

The first task for definition of the control law is to obtain the estimation transfer functions, which allow a time-domain prediction of the fluctuations obtained from upstream measurements. In the present scenario, where linearity is assumed, one has to consider the frequency-dependent growth rates and phase speeds of the dominant mode in order to allow for an accurate prediction. This is done by following PSE-based transfer functions; however, alternative methods could be also used, such as ARMAX [22] or by the direct application of local linear stability theory [35].

Linear PSE can be thought of as a computationally efficient way to obtain the solution of a parabolized boundary value problem in the frequency domain, approaching the solution of the linearized Euler or Navier–Stokes systems. An upstream condition, taken for instance at $x = 0$, is marched downstream. Such condition, given in the first point of the domain, is normally taken from a locally parallel computation, and a single unstable eigenmode is then considered, as outlined in "Appendix". The implementation of PSE also involves the determination of a local wave number $\alpha(x)$, iteratively found to respect an auxiliary condition; this procedure renders nonlinearity to the model. This removes the streamwise exponential dependence of the shape functions. It should then be noted that two PSE solutions with two different eigenmodes as inflow condition can be superimposed to obtain an approximated solution of the original linearized system. However, such superposition will not be a solution of the PSE problem as the local wavenumber will be a priori different as PSE would tend to converge to one of them. Thus, the method is only capable of tracking a single mode, which therefore means that for a system with more than one unstable mode, performing the superposition is not straightforward. This problem is tackled, for example, in the work of Sinha et al. [43] for a dual-stream jet which has two unstable eigenmodes; dedicated PSE computations are then performed for each one of them. In the current problem, however, the flow is dominated by the Kelvin–Helmholtz instability which makes the PSE method a suitable approach to obtain transfer functions, as it will be demonstrated next, with a low computational cost.

Furthermore, PSE allows for a calculation where only the mean flow is required for the construction of the reduced-order models, which are given in terms of transfer functions. Once such transfer functions are available, the predictions are made in terms of a convolution, which is an inexpensive procedure. These characteristics allow for a fast exploration of the control parameters, such as positions, spacing between units; a priori, these would not be directly available using more empirical methods based on system identification, which were shown to present similar performances in estimating the flow quantities in another study by this group [40].

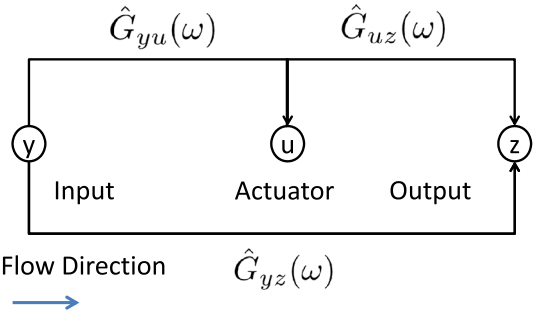

Fig. 2 Scheme for the estimation ($\hat{G}_{yu}$ and $\hat{G}_{yz}$) and actuation ($\hat{G}_{uz}$) transfer functions

The estimation techniques have been developed previously in Sasaki et al. [40] and will be briefly summarized here for the sake of clarity. The linearity of the PSE may be exploited in order to obtain a single-input–single-output model between any given pair of positions along the flow and considering any of the dependent variables (pressure, vertical or horizontal velocities, for this particular problem). Prior to the computation of the PSE, it is necessary to account for a baseflow (taken here as the mean flow) which, for the two-dimensional case, is a function of the axial and transverse coordinates. A mild streamwise variation is then a necessary hypothesis for the parabolization of the equations. This assumption permits the PSE decomposition into a slowly varying shape function and a fast wave-like part. The mean flow is obtained from a previous DNS, exciting the flow with broadband perturbations and allowing the initial transients to seize. PSE can then be used to calculate the fluctuations for a wide range of frequencies, which is feasible due to the low computational cost of this method.

Defining the complex quantities $\hat{Y}(\omega)$ and $\hat{Z}(\omega)$ of two positions along the flow considered respectively as an input and an output, and measured at the positions (X_y, Y_y) and (X_z, Y_z), as presented in the scheme in Fig. 2, with ω defining the angular frequency, and assuming a linear relation between these, a frequency-domain transfer function may be written as:

$$\hat{G}_{yz}(\omega) = \frac{\hat{Z}(\omega)}{\hat{Y}(\omega)}. \tag{3}$$

where upper-case letters and the hat symbol denote Fourier-transformed quantities, in the frequency domain; their time-domain counterparts are written with corresponding lower-case letters. A convolution kernel, that we denote *time-domain transfer function*, is readily available from the inverse Fourier transform of $\hat{G}_{yz}(\omega)$;

$$g_{yz}(t) = \frac{1}{2\pi} \int_{-\infty}^{\infty} \hat{G}_{yz}(\omega) \mathrm{e}^{-i\omega t} \, \mathrm{d}\omega. \tag{4}$$

From $g_{yz}(t)$, which is a real quantity written in the time domain, the output $z(t)$ may be estimated from measurements of the input $y(t)$, which defines a SISO system as

$$z(t) = \int_{0}^{\infty} g_{yz}(\tau) y(t-\tau) \, \mathrm{d}\tau. \tag{5}$$

where it is assumed that $g_{yz}(\tau) = 0$ for $\tau < 0$, i.e. the transfer function is *causal*. A causal transfer function for estimation is a necessary assumption for an online prediction of the output, based on past and present information. This is expected if the output z is taken for a position downstream of the input y, since the mixing layer is characterized by a convective instability [26].

The use of PSE for reduced-order modelling implies that only the Kelvin–Helmholtz (K–H) mode is tracked. This mode is expected to dominate the dynamics of mixing layers and jets, an underlying assumption which can be verified by comparison of the reduced-order model with DNS results. Furthermore, it has been recently shown [40] that PSE-based transfer functions may be used for the modelling of a high-Reynolds turbulent jet, with compelling correlations as long as input and output positions are within the initial shear layer of the jet, where the K–H mode is spatially unstable. In the same study, the performance of PSE-based TFs was demonstrated to be comparable to two more empirically dependent techniques, providing further evidence of its suitability for this sort of application.

Non-modal effects are not a priori captured, which means that this method could not be directly used for transient effects seen for instance in bypass transition in boundary layers. The work of Levin and Henningson [33] demonstrates how to modify PSE to account for transient growth, via the use of an optimal disturbance, derived using the adjoint equations. Such method could in principle be applied to the derivation of transfer functions targeting non-modal effects. This is, however, out of the scope of this paper; here only the modal stability properties will be investigated.

An example of the prediction is shown in Fig. 3, where the PSE prediction is compared to the transverse velocity fluctuation from a nonlinear DNS run at the position of $(X_z, Y_z) = (100, 0)$, the input position of $(X_y, Y_y) = (75, 0)$ was considered for the TF. We observe close agreement between the predictions from the PSE-based TF and the DNS results. Only the behaviour of linear wavepackets is predicted with Eq. (5) and a deterioration of the comparisons between such prediction and the actual outputs of the DNS is expected as one moves downstream.

Figure 4 presents a $X - Y$ mapping of the correlation at $\tau = 0$ between prediction (z_{est}) and measurement (z_{DNS}), as defined in Eq. (6),

$$C(X_z, Y_z) = \frac{\int_{-\infty}^{\infty} z_{\text{DNS}}(t) z_{\text{est}}(t) \mathrm{d}t}{\sqrt{\int_{-\infty}^{\infty} z_{\text{DNS}}^2(t) \mathrm{d}t} \sqrt{\int_{-\infty}^{\infty} z_{\text{est}}^2(t) \mathrm{d}t}} \tag{6}$$

where prediction is done with a fixed input position, located at $(X_y, Y_y) = (75, 0)$. Correlations close to one indicate an accurate prediction and validate this method.

One of the advantages of the PSE transfer function method is that it allows for the direct derivation of a multiple-output system, obtained by simply calculating the transfer function between a given fixed input and several downstream outputs. The low computational cost of the method again allows for such a prediction, as once the TFs have been built, only a convolution is necessary to perform the prediction. Figure 5 shows some sample results, where the measurements at $(X_y, Y_y) = (100, 0)$ are used as the input data.

Alternatively, one could proceed empirically by building the transfer function using broadband inflow perturbations in the numerical simulation. This method, which is based on the frequency response between inputs and outputs [5] is outlined in Sasaki et al. [40] and will not be pursued here.

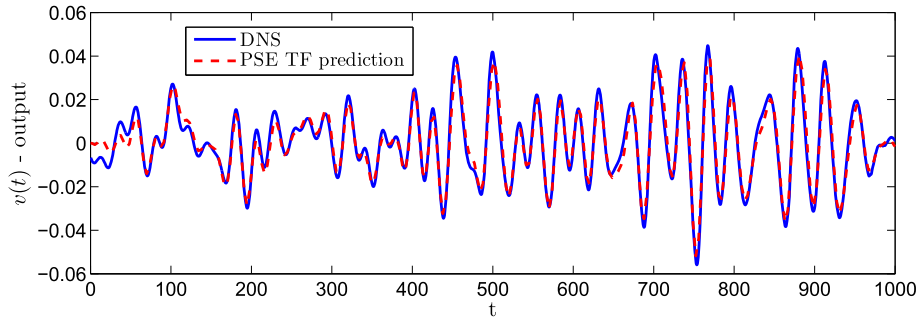

Fig. 3 Comparison of the PSE predictions against a DNS run for the $v(t)$ transverse velocity component

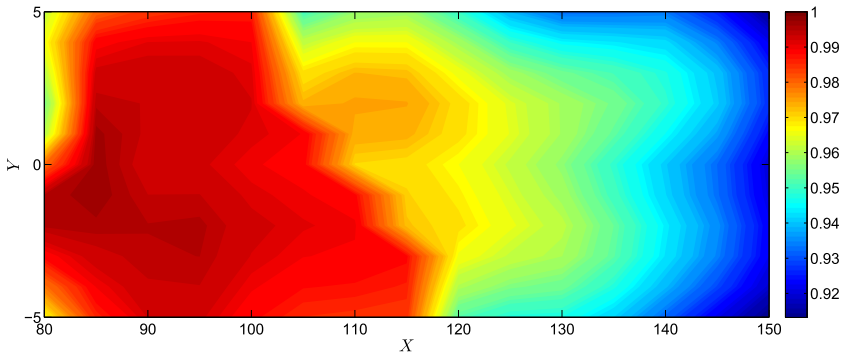

Fig. 4 Correlation map for the prediction of $v(t)$, using the PSE transfer function as a reduced-order model and the input located at $(X_y, Y_y) = (75, 0)$

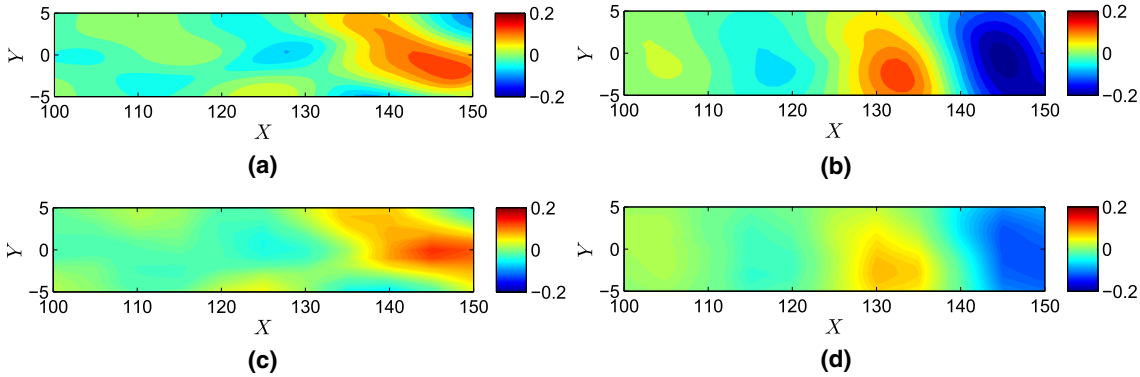

Fig. 5 Results of the direct numerical simulation in comparison with PSE transfer function predictions for axial and transverse velocity fluctuations. **a** DNS—axial velocity fluctuation, **b** DNS—transverse velocity fluctuation, **c** PSE TF prediction—axial velocity fluctuation and **d** PSE TF prediction—transverse velocity fluctuation

3.2 Actuation

Before closing the loop and defining a control law, it is necessary to determine how a given actuation will affect the behaviour of the fluctuations downstream. The DNS can be conveniently excited by a body force in the form

$$f(X, Y, t) = u(t)\mathrm{e}^{-\frac{(X-X_u)^2}{L^2}}\mathrm{e}^{-\frac{(Y-Y_u)^2}{L^2}} \tag{7}$$

where L determines the spatial support of the applied body force, and $u(t)$ gives the time behaviour of the perturbation, which is supposed to present a broadband spectrum in order to act over all the unstable frequencies of the flow. The expression in Eq. (7) can be used to define actuations f_X or f_Y in either X or Y directions. In this work, we have used $L = 5$ and tested different actuation positions (X_u, Y_u).

We need to determine theoretically how actuation excites flow fluctuations. This has been studied in some detail by Hill [23]. Here, it is necessary to project the body force, at the position of the actuator, onto the Kelvin–Helmholtz mode. This idea is based on the signalling problem, described in Huerre et al. [24] and Huerre and Monkewitz [25,26]. The procedure provides the amplitude of the Kelvin–Helmholtz mode at the position of the actuator, which is then used as an initial step for the PSE marching procedure.

In accordance with the assumptions of PSE, the flow is considered locally parallel close to the disturbance; one may then use this hypothesis to obtain the resulting amplitude of the K–H mode and march it downstream using PSE. The force is expected to result in a projection onto several different modes. However, as only the K–H is unstable, after a certain spatial transient, only its contribution will remain downstream, as amplitudes of other modes decay to zero. As shown in "Appendix 2", flow fluctuations are given as

$$\hat{\hat{\boldsymbol{q}}}(\alpha, Y, \omega) = i\langle\hat{\hat{\Psi}}_{\mathrm{KH}}(\alpha, Y, \omega),\, \hat{\hat{f}}(\alpha, Y, \omega)\rangle\mathrm{e}^{i\alpha_{\mathrm{KH}}X_u}\hat{\hat{\phi}}_{\mathrm{KH}}(\alpha, Y, \omega) \tag{8}$$

where the double hat denotes a Fourier transform in space from X to the wavenumber α and time from t to ω, $\hat{\hat{\phi}}_{\mathrm{KH}} = (\hat{\hat{u}}, \hat{\hat{v}}, \hat{\hat{p}}, \alpha\hat{\hat{u}}, \alpha\hat{\hat{v}})$ and $\hat{\hat{\Psi}}_{\mathrm{KH}} = (\hat{\hat{u}}, \hat{\hat{v}}, \hat{\hat{p}}, \alpha\hat{\hat{u}}, \alpha\hat{\hat{v}})^*$, $*$ indicating adjoint variables, are respectively the direct and adjoint Kelvin–Helmholtz modes, calculated from the locally parallel problem, with corresponding wavenumber α_{KH} and $\langle , \rangle$ indicates the inner product between two quantities. Equation (8) provides the velocity and pressure fluctuations associated with the actuation near its position. These can be treated as initial conditions for PSE, which are marched downstream following the usual procedure. The transfer function is then calculated using the formalism presented in Sect. 3.1, with input taken as $\hat{u}(\omega)$, measured at the position (X_u, Y_u).

A comparison of the time series between nonlinear simulation and prediction is shown in Fig. 6, at the position $X_z = 125$, for a forcing located at $X_u = 100$. The correlation map is presented in Fig. 7 and exhibits an adequate behaviour, with correlations above 85%, providing a validation of this procedure.

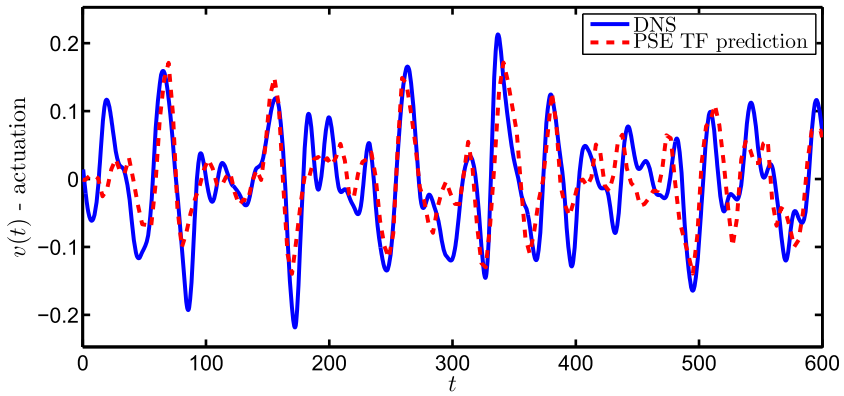

Fig. 6 Comparison of the PSE prediction and DNS run at the position $X_z = 125$. The actuator is located at X_u=100

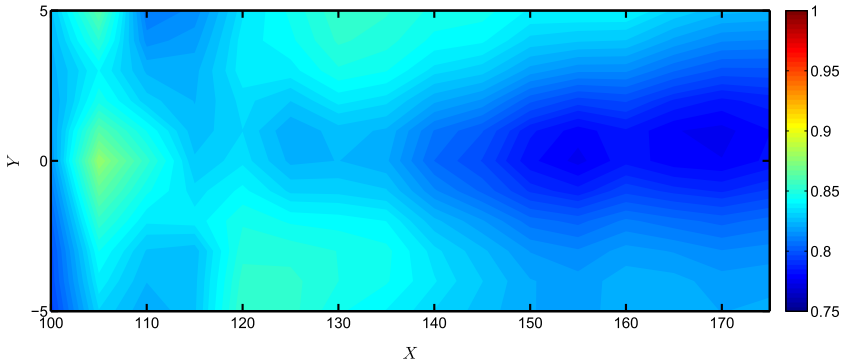

Fig. 7 Correlation map for the actuation transfer function calculated using PSE. A similar behaviour is observed with the empirical model

4 Feedforward and feedback control strategies

Once the estimation and actuation transfer functions have been validated, all the ingredients necessary for closed-loop control of the fluctuations are readily available. Disturbances measured by a sensor will be considered as an *input* $y(t)$ and these are amplified as they are convected downstream. The objective of the actuation is to minimize the *output* $z(t)$ at a fixed position downstream of the actuating signal.

The frequency-dependent phase speeds and growth rates of the instability waves are automatically considered in the transfer functions derived in Sects. 3.1 and 3.2 and two control schemes may result, depending on the relative position between the actuator and sensor. If the actuator is downstream of the input, for a convectively unstable flow, its effect on the upstream sensor is negligible [4] and the resulting block diagram for closed-loop control is shown in Fig. 8. The output $z(t)$ is then directly obtained from the superposition of an open-loop behaviour with an actuating signal, and a scheme denoted as *disturbance feedforward* [41] results, with the objective of rejecting incoming disturbances, measured at $y(t)$. The closed-loop control of such amplifier flow [26] may be understood in terms of the actuation leading to a perturbation profile in phase opposition with the unperturbed, open-loop behaviour of the system, causing a cancellation of the incoming wave.

It should be noted that a feedforward gain alone is incapable of changing the stability characteristics of the system since it is unable to change the eigenvalues of the original plant [17,44]. In spite of this fact, its use is appropriate for globally stable but convectively unstable flows, such as the mixing layer under study, which does not present unstable eigenvalues. For this type of application, the feedforward gain acts with the objective of rejecting incoming disturbances. For the stability characteristics of feedforward control laws, the reader is referred to the works of Fabbiane et al. [17] and Belson et al. [4], for a fluid dynamics perspective and the work of Devasia [14] for an overview of feedforward controllers with a more system-oriented guidance.

Consider now the case where the actuation signal affects the input sensor (e.g., for this convective flow this would happen if the actuation was positioned upstream of the input sensor); The resulting scheme is said

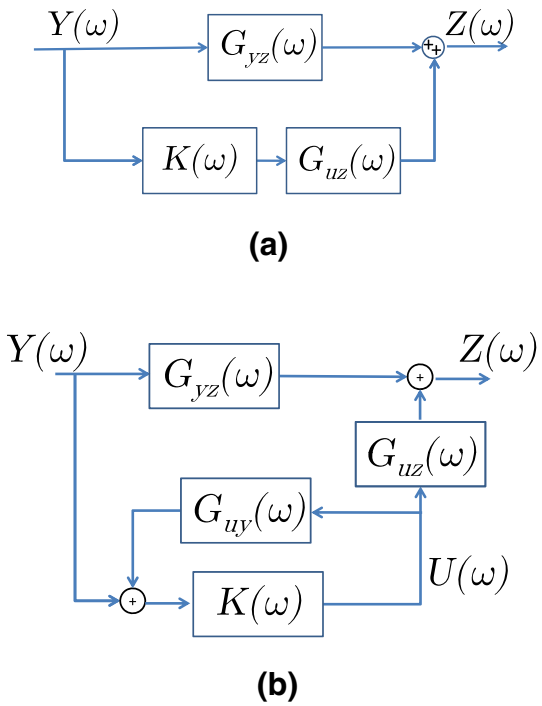

Fig. 8 Block diagram for **a** feedforward and **b** feedback control laws. $\hat{G}_{yz}$ and $\hat{G}_{uz}$ are the estimating and actuation transfer functions between input/acting positions and output, respectively. It should be noted that the branch where the transfer function $\hat{G}_{uy}$ is located is added in the feedback scheme, which accounts for the effect of the actuation into the input sensor. The frequency-dependent gain $\hat{K}(\omega)$ is designed separately for each configuration

to be feedback control, since a path for information to flow from the actuation into the input is added. The resulting block diagram for this problem is shown in Fig. 8b.

The resulting outputs, in the frequency domain, are given in Eqs. 9 and 10 below.

$$\hat{Z}(\omega) = [\hat{G}_{yz}(\omega) + \hat{K}(\omega)\hat{G}_{uz}(\omega)]\hat{Y}(\omega) \tag{9}$$

$$\hat{Z}(\omega) = \left[\hat{G}_{yz}(\omega) + \frac{\hat{K}(\omega)\hat{G}_{uz}(\omega)}{1 - \hat{K}(\omega)\hat{G}_{uy}(\omega)}\right]\hat{Y}(\omega) \tag{10}$$

which refer to feedforward and feedback control, respectively. Feedback control is known to present lower performances, when compared to feedforward, when applied to convectively unstable flows [4]. The reasons for such behaviour will be explored further in this work.

For both cases, the resulting gains are frequency dependent and are calculated such that $\hat{Z}(\omega) = 0$,

$$\hat{K}(\omega) = -\frac{\hat{G}_{yz}(\omega)}{\hat{G}_{uz}(\omega)} \tag{11}$$

$$\hat{K}(\omega) = -\left[1 - \hat{G}_{uy}(\omega)\frac{\hat{G}_{yz}(\omega)}{\hat{G}_{uz}(\omega)}\right]^{-1}\frac{\hat{G}_{yz}(\omega)}{\hat{G}_{uz}(\omega)} \tag{12}$$

corresponding to the feedforward and feedback gains, respectively. It should be observed that when there is no feedback between actuation and input (i.e. $\hat{G}_{uy}(\omega) = 0$), the feedback gain reduces to the feedforward one.

The actuation is given, in the time domain, as a convolution of the gain with the input:

$$u(t) = \int_{-\infty}^{\infty} k(\tau)y(t-\tau)\,\mathrm{d}\tau, \tag{13}$$

where $k(t)$ is the inverse Fourier transform of $\hat{K}(\omega)$.

This can only be accomplished in practice if $k(\tau)$ is causal, i.e. $k(\tau) = 0$ for $\tau < 0$, since in this case only present and past sensor information are used to decide present actuation. As will be seen shortly, this is the case when the actuator is placed downstream of the sensor. Moreover, the compensator $k(\tau)$ tends to zero for sufficiently large τ, and in practice the convolution in Eq. (13) can be approximated by

$$u(t) = \int_0^T k(\tau) y(t-\tau) \mathrm{d}\tau. \tag{14}$$

Furthermore, T will define the number of samples to be stored before the actuation starts. In practical terms, it corresponds to the length of the numerically calculated $k(t)$.

The procedure for calculating the gain $\hat{K}(\omega)$ in Eq. 9, for feedforward control, is referred to as an inversion and should be performed over the controllable frequencies, avoiding zeros of $\hat{G}_{uz}(\omega)$. In other words, high frequencies, where the linear model is not representative of the behaviour of the system should be avoided, such that eventual noise is not amplified, which would degrade the efficiency of the control law. In the work of [14] a strategy to penalize the actuation, in the frequency domain, is proposed for a feedforward control law, which avoids high actuations in the aforementioned frequencies. Through this paper, however, it was chosen to low-pass filter the resulting gain prior to the implementation in the closed-loop system. Differently from applications of feedforward control in system's theory [38], the control action is based in measurements of the actual state of the system and calculated such that actuation leads to a destructive interference of the incoming instability wave. This is obtained by the aforementioned superposition of the incoming, open-loop, wave with the actuating signal, obtained from the inversion of the system. This method for calculating the feedforward gain is known to be effective when the uncontrolled system presents a BIBO (bounded-input–bounded-output) stability, which in turn will lead to a bounded actuation [15], as is the case of the system under study.

It is noteworthy that, in spite of sharing some common objectives, the feedforward and feedback control laws derived in this section should not be regarded as "zero-pole" cancellations. Such zero-pole compensators would act as multiplicative transfer functions, rather than the superpositions shown in Fig. 8 and should be avoided as they may lead to instabilities and robustness issues [38]. Given that the system is already globally stable, it would be desirable to consider a control law which does not change its stability characteristics, which may be obtained by the feedforward scheme proposed here.

5 A baseline case for control

We start by considering a baseline case for control, using the feedforward configuration. Sensors and actuation will be placed in the centre of the flow, separated by an axial position of $\Delta = 25$. This case will be used for comparisons with different relative positions between input, actuation and output and transverse locations for actuation.

The axial positions will be determined from the peak correlations between nonlinear simulation and the reduced-order model prediction, as defined in Eq. 6. The control signal is expected to be more effective in regions of high values of this parameter, which indicate where the linear model gives a good estimation of the nonlinear dynamics.

Figure 9 presents the peak correlation for both estimation and actuation transfer functions, at four different inputs and four outputs, separated by $\Delta X = 25$. For both estimation and actuation transfer functions, we observe that predictions lose accuracy with increasing distance and that use of downstream inputs also leads to a decrease of correlations between predictions and DNS results. Specifically, we observe that when the input or actuation is taken at $X = 130$ and higher, the correlations between prediction and DNS results worsen, particularly for the actuation transfer function. Both trends can be attributed to nonlinearity, as the evolution of the mixing layer leads to vortex roll-up and pairing which can only be approximately accounted for by the linearized model [11].

The basic idea is then to choose a set of positions where the flow dynamics is mostly linear, such that the linear control laws derived previously may be used. The effect is then tested in a nonlinear simulation where we assess whether the vortex roll-up and shedding is delayed by control action. This approach is standard on flow control problems; for instance Fabbiane et al. [16] present an application to a boundary layer, where all the control action is performed upstream of the transition location, such that the flow dynamics is predominantly linear. Alternatively, application of an actuation in the vortex roll-up region, where the Kelvin–Helmholtz mode has saturated, would probably be less efficient and require the use of nonlinear techniques, which are

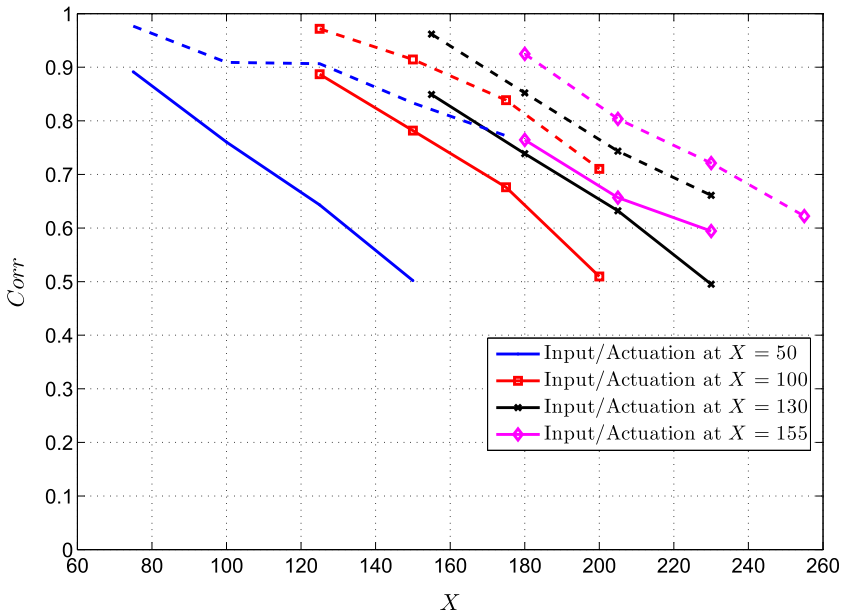

Fig. 9 Peak correlation between prediction and DNS for the estimation and actuation transfer functions. Solid and dashed lines represent the correlations obtained for the actuation and estimation transfer functions, respectively. The input or actuation was located at $X = 50$, 100, 130 and 155, in the center line of the flow

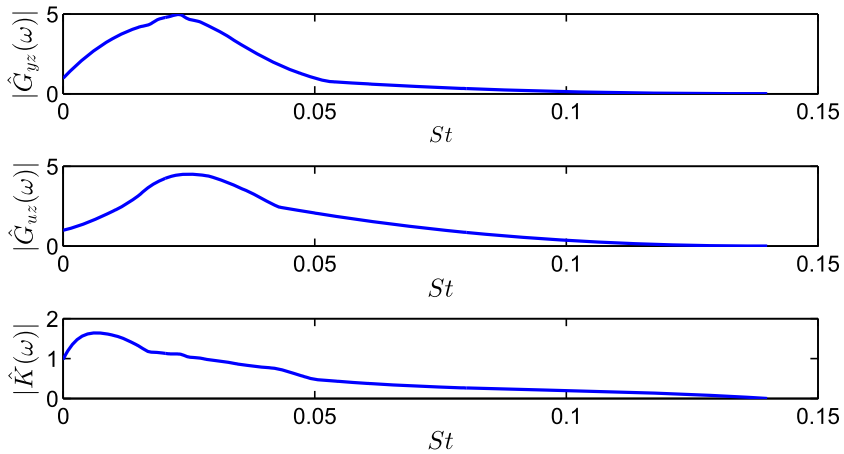

Fig. 10 Resulting actuation transfer functions between estimation, actuation and output and computed gain for compensator. Subscripts *y, u, z* define input, actuation, and output positions, localized at $X = 75$, 100 and 125, respectively, and at the centerline of the flow, considering the axial velocity fluctuation. The actuation corresponds to a transverse forcing

outside scope of this paper. The set of positions for closed-loop control were then chosen to be $X = 75$, 100 and 125, all of which taken in the centreline of the flow, for input, actuation and output, respectively $((X_y, Y_y)$, (X_u, Y_u) and $(X_z, Y_z))$.

The behaviour of the transfer functions and resulting inversion gain in the frequency domain are shown in Fig. 10. By considering the actuation transfer function, $\hat{G}_{uz}(\omega)$, it is noticeable that its amplitude decays substantially for Strouhal numbers higher than 0.05, such that for $St > 0.1$ $\hat{G}_{uz}(\omega)$ it is close to zero, determining a threshold for the controllable frequencies of the problem. The gain is also low-pass-filtered for higher frequencies than $St = 0.1$.

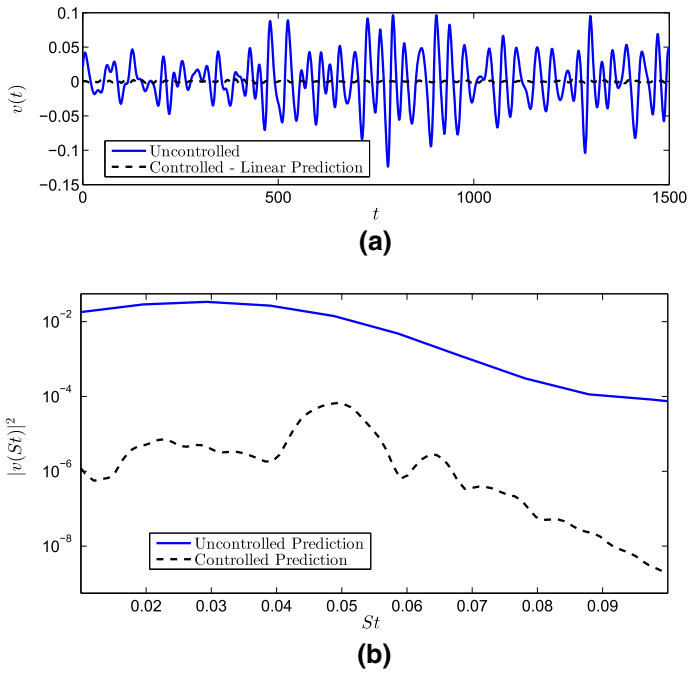

Fig. 11 Closed-loop behaviour for the linearized system using wave cancellation in the **a** time and **b** frequency domain

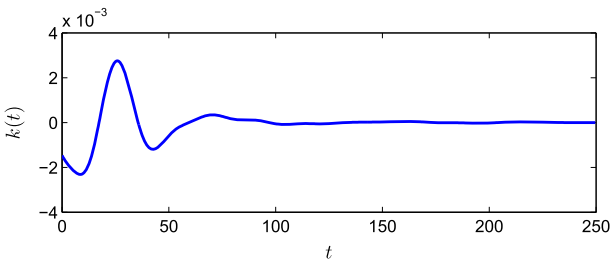

Fig. 12 Kernel for the positions and input/outputs corresponding to the baseline case

5.1 Results for the linearized system

Prior to testing of the gains in the nonlinear direct numerical simulation, the closed-loop behaviour was evaluated in the linearized system, described in terms of transfer functions—Eq. (9). Figure 11 shows the resulting output, for the wave cancellation, along with the power spectral density. The control was targeting the transverse velocity fluctuation. A significant reduction is observed, both in the time and frequency domains, and we have observed the RMS values of the transverse velocity fluctuations were reduced by 40 times in comparison to the open-loop case.

5.2 Application to the direct numerical simulation

The control laws and gains described in the previous section were implemented in the direct numerical simulation of the mixing layer, which comprises nonlinear behaviour. The simulation considers a broadband frequency input which therefore includes non-periodic vortex roll-up and pairing, and thus a much more challenging task for the controllers than the linearized system.

For implementation, Eq. (13), for the actuation, is discretized, integration being limited to a maximum τ that includes 200 times. This value is used to correctly capture the wavepacket-like shape of the kernel, in the time domain, as shown in Fig. 12. The input, actuation, and objective positions are the same tested in the linear framework (75, 100, and 125, respectively), all on the centerline of the flow.

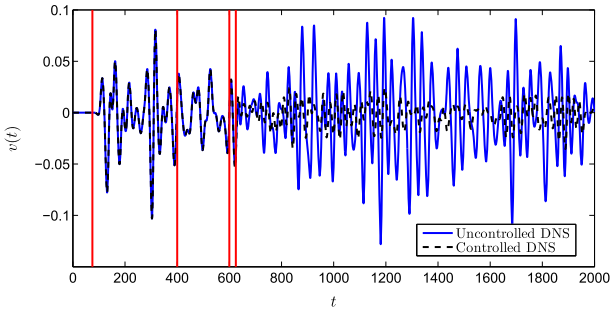

Fig. 13 Comparison of the uncontrolled simulation against the controlled case, for the transverse velocity fluctuation. The vertical lines indicate the time to the fluctuation to reach the output, transient, buffer and time to reach the objective, respectively

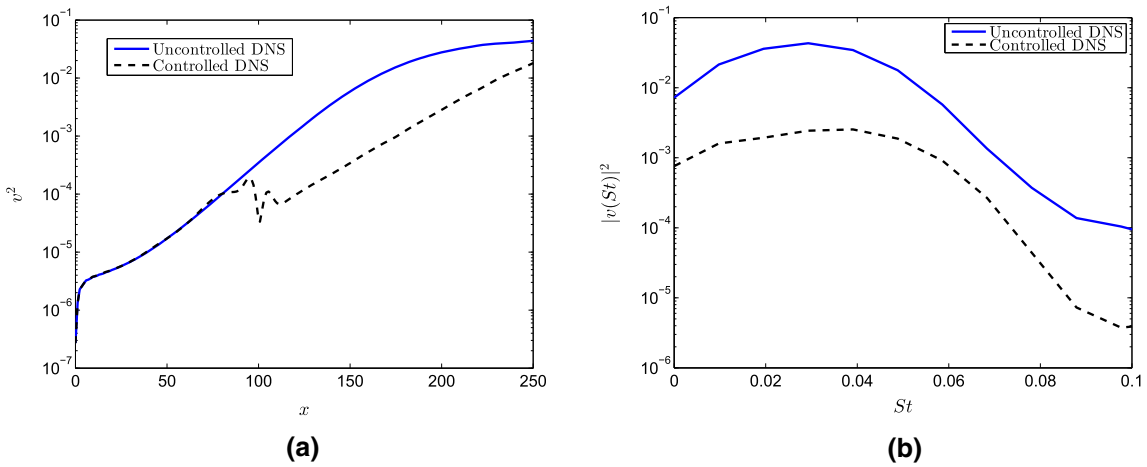

Fig. 14 **a** Mean-squared value for the transverse velocity fluctuation in the centerline of the flow. **b** Power spectral densities of the uncontrolled and controlled nonlinear simulations for the transverse velocity fluctuation at the objective position

Figure 13 shows the resulting velocity fluctuation at the objective position. The time signal at the position of the objective may be split in the following way; initially the fluctuations are null as the perturbations introduced in the inflow have not yet reached the downstream areas. There is a transient which is disregarded to allow the flow to establish and a buffer of 200 cumulative timesteps is stored to compute the actuation. After this time, it is observed that the actuation is effective in reducing the amplitude of v. Albeit not shown here, we also observe that the u component is also attenuated.

In order to compute the reductions observed in closed-loop system in a more quantitative manner, a plot of the mean-squared (MS) value of the transverse velocity fluctuation along the centerline of the flow is shown in Fig. 14a. Reductions in the velocity fluctuations are observed not only at the objective position, but also for a considerable downstream distance. The Kelvin–Helmholtz mode leads to strong exponential growth in all cases, but closed-loop control allows for a reduction of more than one order of magnitude of the objective fluctuation. The resulting power spectral densities (PSD) for the nonlinear simulation, at the objective position are presented in Fig. 14a. As expected, significant PSD reductions are obtained at the frequencies where the K–H mode is unstable, which justifies its use within the PSE transfer functions framework.

The differences between the closed-loop control applied to the linearized (transfer function description) and nonlinear simulation (Figs. 11 and 14) are related to slight inaccuracies of the PSE transfer functions in capturing the behaviour of the flow, and also to nonlinearities present on the DNS. Such inaccuracies are predominantly present in the actuation transfer function, which assumes the flow to be locally parallel in the position of the actuator, an underlying hypothesis to project the forcing into the K–H mode. In spite of this, the large reductions observed in the nonlinear case demonstrate that PSE is an adequate reduced-order model for this flow, which justifies its use for control. Empirically derived transfer functions [40] obtained using system identification techniques presented comparable performances in the closed-loop simulation, and these results will not be shown here for the sake of brevity.

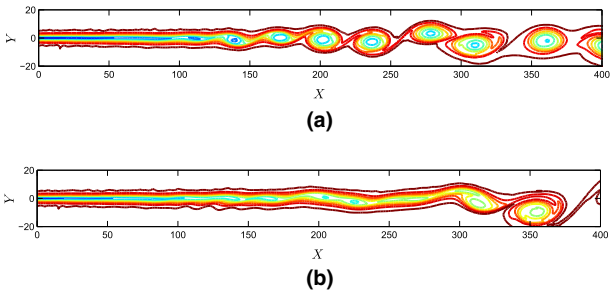

Fig. 15 Comparison of the vorticity fluctuations for the uncontrolled **a** and controlled **b** cases at $t = 1200$. The delay in the vortex pairing becomes apparent

Finally, vorticity snapshots of the uncontrolled and system inversion controlled cases are presented in Fig. 15. As the control action takes place, vortex roll-up and pairing is delayed. This supplies evidence that for the analogous compressible mixing layer problem [11,12,48] or low Reynolds number jet [37,47] the control action would result in lower sound radiation.

6 Robustness evaluation

The robustness of the inversion feedforward controller was evaluated with respect to the variations of the following parameters:

- Reynolds number: The control law was designed for the fixed value of $Re = 100$, and it was evaluated via simulations at different values of this parameter. This seeks to evaluate how plant uncertainties affect the closed-loop system.
- Amplitude of the inflow perturbations: In the linear framework, the models are independent of the considered inflow amplitude such that the control laws are designed independently of this parameter. In the nonlinear simulation however, by increasing the amplitude of the inflow perturbations, nonlinear effects could appear more prominently, which would in turn affect the linearly designed control laws. The amplitude of the initial perturbation was normalized by the value of Amp_0, a reference amplitude chosen such that the flow exhibited a linear behaviour at this condition.
- Unsensed noise: Perturbations in the form of a body force, with the same Gaussian support as the actuation, were inserted at $X = 115$, downstream of the actuator position (the same analysis was made when the forcing was between input and actuator and similar results were obtained).
- White noise in sensors and actuators: White noise was inserted in measurement and actuation signals,

$$y(t) = y_{\text{real}}(t) + A_{\text{noise}}\omega_l(t) \tag{15}$$

$$u(t) = u_{\text{real}}(t) + A_{\text{noise}}\omega_l(t) \tag{16}$$

where y_{real} and u_{real} represent the noiseless values of the measurement and actuation parameters, A_{noise} the amplitude considered for the noise and ω_l is a broadband signal, such that $\overline{\omega_l^2} = 1$. The noise amplitude was chosen in order to result in a given signal-to-noise ratio, $\text{NTS}_y = \overline{y_{\text{real}}^2}/A_{\text{noise}}^2$ and $\text{NTS}_u = \overline{u_{\text{real}}^2}/A_{\text{noise}}^2$ for measurement and actuation, respectively. The objective is to model a more realistic experimental implementation, where environmental noise could be present and could affect sensing and actuation.

We have chosen for this evaluation to consider the baseline configuration of Sect. 5, with sensor, actuator and output placed respectively at $(X, Y) = (75, 0)$, $(100, 0)$ and $(125, 0)$. As in previous sections, the objective of the controller was to attenuate the transverse velocity fluctuations.

Figure 16 presents the quotient between the MS signals of the controlled and uncontrolled cases for the transverse velocity fluctuations. It is observed that the system is fairly insensitive to the amplitude of the inflow perturbations, provided that the dynamics remain predominantly linear for the evaluated amplitudes, Reynolds number variations and noise in sensors and actuators. The same behaviour was observed when measurement noise was included, which is expected given that the actuation is directly related to the measurement via the convolution of Eq. 14.

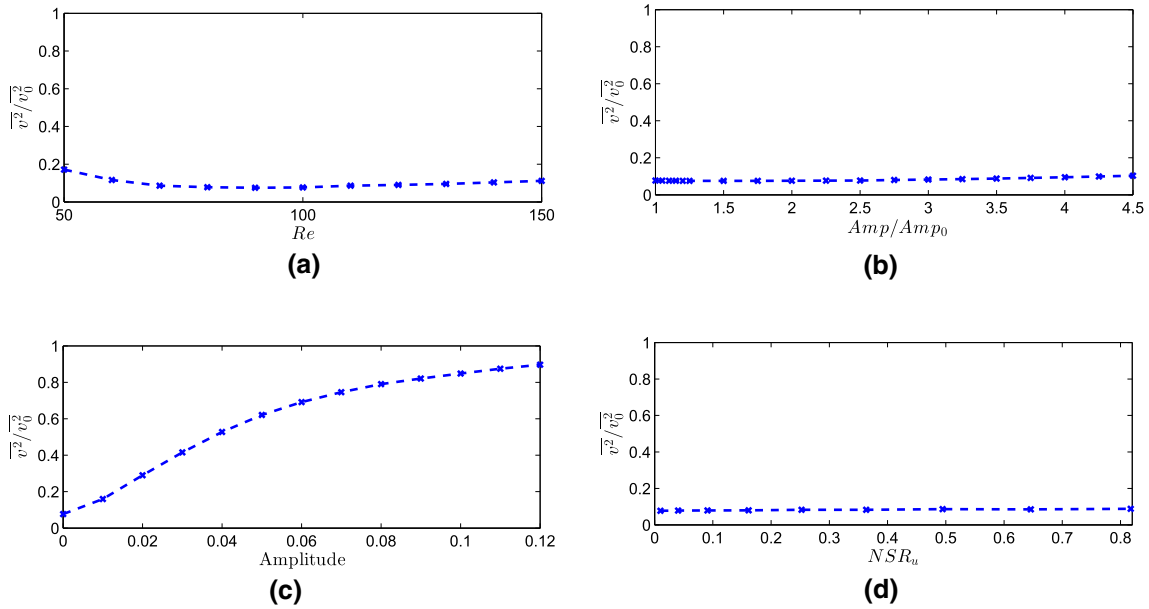

Fig. 16 Robustness evaluation of the inversion controller, MS of the transverse velocity components of the controlled case divided by the corresponding open-loop scenario. **a** Reynolds number variation (control laws were designed for $Re = 100$), **b** amplitude of the inflow perturbations divided by their nominal value, **c** amplitude of the perturbations inserted between input and output positions, **d** noise in the actuation signal (a similar behaviour was observed for the case of measurement noise and will not be shown here, for the sake of brevity)

Unsensed perturbations, however, rapidly cause the performance of the inversion controller to degrade. This is a known behaviour of feedforward controllers and has been recently tackled in the work of [18] via an adaptive method, using the same feedforward scheme considered here.

7 Effect of the transverse and axial positions of actuation

A manner to consider a priori an appropriate position for actuation is to project a forcing with the shape of a Dirac delta function $f(X, Y) = \delta(X - X_u)\delta(Y - Y_u)$, such that $\hat{\hat{f}} = \delta(Y - Y_u)\mathrm{e}^{-i\alpha X_u}$, given the definition of the Fourier transform and the filtering property of the delta function. For this case, projection of the forcing onto the Kelvin–Helmholtz mode will result exclusively in the adjoint mode at $Y = Y_u$ multiplied by an exponential, as per Eq. (17).

$$\langle \hat{\hat{\Psi}}_{\mathrm{KH}}(\alpha, Y, \omega), \hat{\hat{f}}(\alpha, Y, \omega)\rangle = \hat{\hat{\Psi}}_{\mathrm{KH}}(\alpha, Y, \omega)\mathrm{e}^{-i\alpha_{\mathrm{KH}}X_u}. \tag{17}$$

Such that, as shown in "Appendix 2", the effect of this forcing at a given position X, downstream of it, will depend exponentially on the distance:

$$\hat{\boldsymbol{q}}(X, Y, \omega) = \hat{\hat{\Psi}}_{\mathrm{KH}}(\alpha, Y, \omega)\mathrm{e}^{i(X-X_u)\alpha_{\mathrm{KH}}}\hat{\hat{\phi}}_{\mathrm{KH}}(\alpha_{\mathrm{KH}}, Y, \omega) \tag{18}$$

Therefore, it would be expected that appropriate places to define the actuation and objective positions would be respectively at the inflow position, such that the amplification of the control is highest, and downstream of the stabilization region of the K–H mode due to the thickening of the mixing layer (sometimes referred to as branches I and II of the neutral stability curve [22]).

However, at these positions, the reduced-order models considered would be ineffective in predicting the behaviour of the flow. Close to the entrance of the domain and further downstream, where nonlinear effects start to occur, the PSE and empirical TFs are unable to predict effectively the behaviour of the nonlinear simulation. We therefore proceed by choosing a set of positions along the axial direction which is in line with the expected accuracy of the considered models. The correlation between DNS and linear predictions provides a good estimate for such, as shown in the previous section.

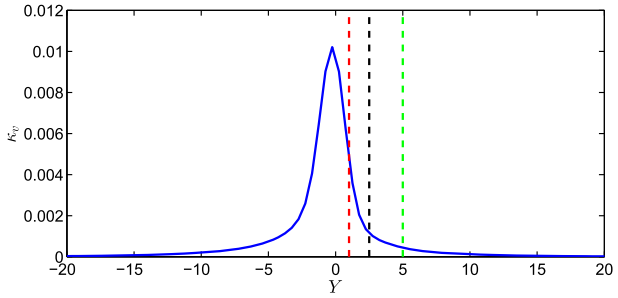

Fig. 17 Sensitivity index for transverse forcing aiming at v, vertical lines indicate other transverse positions that were considered in Fig. 18, for comparison with the optimal case

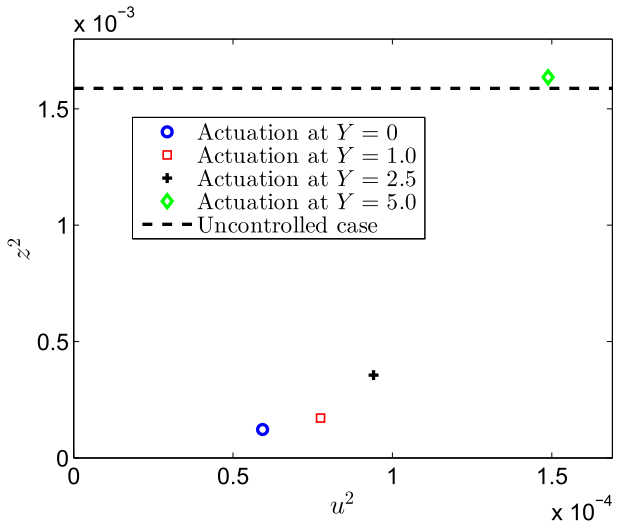

Fig. 18 Comparison of the mean square values for the objective and actuation signals at four different transverse positions, at $X_u = 100$. The dashed line indicates the MS of the output for the open-loop case

As for the transverse direction dependence, it may be extracted from Eq. 17, as it corresponds to finding the $\delta(X - X_u)\delta(Y - Y_u)$ response of the system. Defining parameter κ_v,

$$\kappa_v = \int_{-\infty}^{\infty} |\hat{\hat{\Psi}}_v(\alpha, Y, \omega)|^2 \mathrm{d}\omega \tag{19}$$

where $\hat{\hat{\Psi}}_v(\alpha, Y, \omega)$ is the adjoint mode at Y_u corresponding to transverse forcing. The greater the value of this parameter, the more efficient will be body force, introduced at Y_u, in producing a response in the controllable frequencies of the problem. Figure 17 presents the value of κ_v, at the position $X_u = 100$, indicating that it is ideal to act along the centerline of the flow, in order to obtain the highest response.

To illustrate the effect of variations of the actuation position along the transverse position, three cases were considered for comparison against the baseline, at Y_u =1.0, 2.5 and 5.0, as highlighted in Fig. 17. Separate control laws were designed for each configuration. Figure 18 shows the comparison of the resulting mean square (MS) of the objective and actuation signals. Moving the actuation away from the centerline, where κ_v presents the highest value, causes the control to become less efficient, leading to higher actuation values and lower performances in terms of the reduction at the objective. For actuation centered at $Y = 5$ we observe that no benefits are obtained by control; it can be said that in this configuration the actuator choice becomes largely inefficient in cancelling the Kelvin–Helmholtz instability at the desired position.

This section serves as a guideline for the determination of appropriate set of positions for placement of sensors and actuators in the flow. The exact determination of optimal sensor and actuator placements would be highly related to the model accuracy, the considered objective and control design. The problem could be addressed in the spirit of the study by Chen and Rowley [10], but is outside of the scope of the present work.

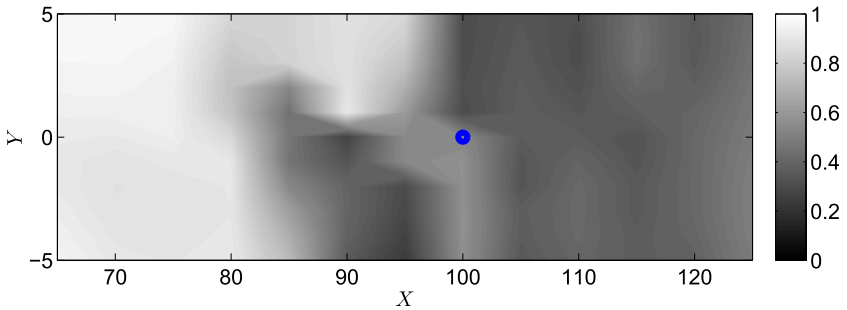

Fig. 19 P parameter for evaluation of the causality of the transfer function. Input is varied and actuation and output positions are fixed at $X_u = 100$ and $X_u = 125$, both on the center line of the flow. The blue circle indicates the actuator's position (color figure online)

8 The role of causality

The actuation signal in Eq. 13 can only be used with $\tau \geq 0$, meaning that only the causal part of the gain can be considered; actuation must be decided using only present and past sensor data. If the gain presents a non-zero value for negative values of τ, information will be lost during the convolution and the efficiency of the controller is therefore expected to decrease.

A suitable choice of positions for input and actuator should then result in a causal gain, to maximize its effect over the actuation. Such information is normally available a posteriori, as in Belson et al. [4], where the gain is evaluated for several positions and analysis of the amplitude of the gain for negative values of t would allow a quantification of causality. An alternative way to perform this task is to use the Hilbert transform [39], which has the added advantage of testing several combinations in a fast, computationally efficient manner. Hilbert transforms are used in the design of causal finite impulse-response filters, which may be implemented in practice. This idea is adopted here to result in causal controllers for flow control implementations.

If the imaginary part of the frequency response (or in this case, a kernel in the frequency domain) of a linear system is equal to the Hilbert transform of the real part, such system represents a causal, linear filter, and knowledge of the real part is sufficient to completely specify the system, the imaginary part adding redundant information. Therefore, a check for causality is to compare the imaginary part of the transfer function with the Hilbert transform of the real part (see Bendat and Piersol [5]).

One way to evaluate this in a quantitative way is to compute the correlation between the Hilbert transform of the real part of the gain, $\hat{H}(\Re(\hat{K}(\omega)))$ and the imaginary part of $\hat{K}(\omega)$. This parameter is given by

$$P = \max\left(\frac{\int_{-\infty}^{\infty} \hat{H}(\Re(\hat{K}(\omega)))\Im(\hat{K}(\omega))\mathrm{d}\omega}{\sqrt{\int_{-\infty}^{\infty} \hat{H}(\Re(\hat{K}(\omega)))^2\mathrm{d}\omega}\sqrt{\int_{-\infty}^{\infty} Im(\hat{K}(\omega))^2\mathrm{d}\omega}}\right). \tag{20}$$

High values of P will indicate a causal gain, which is desirable for control. To evaluate this parameter, actuation and output position were fixed at $(X_u, Y_u) = (100, 0)$ and $(X_z, Y_z) = (125, 0)$, respectively. The position of the input was varied between $75 \leq X_y \leq 125$ and $-5 \leq Y_y \leq 5$, such that when the input is close to actuation or downstream of it, a feedback configuration is reached, where the acting signal affects the input sensor. Figure 19 presents a plot of the resulting parameter P for this region,

If $X_y < 85$, the scheme corresponds to a feedforward configuration, such that the gain is causal and there is no influence of the actuation in the input measurement. On the other hand, if $X_y > 100$, a feedback configuration results, with the input strongly affected by the actuation, as it is downstream of it.

For the region where $85 < X_y < 100$, an intermediary configuration occurs. The flow response to actuation occurs in a slower timescale compared to the natural development of the Kelvin–Helmholtz mode. This is due to the fact that there is an initial transient prior to the development of the K–H instability. Moreover, we observe that if the actuator is placed at negative values of Y the cited transient delay becomes more significant. This could be due to acting in a region with lower local flow velocity. Figure 20 illustrates this effect and the relation with the P parameter, presenting the delay between the measurement of the input and its subsequent effect on the output as a function of X_y, for $Y_y = -5$; such delay is obtained using the peak in the estimation transfer function. This value is compared to the delay between the actuation, at $(X_u, Y_u) = (100, 0)$, and the output measurement, at $(X_z, Y_z) = (125, 0)$, this time obtained using the peak of the actuation transfer

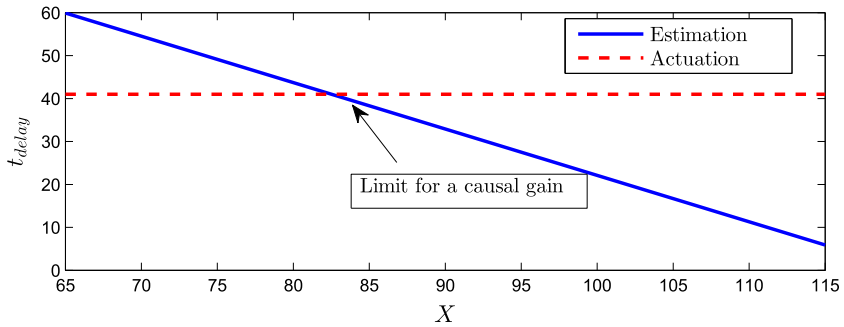

Fig. 20 Comparison between the delay between the measured signal at y and the output (estimation) as a function of the position of the measurement; and the delay between the actuation u and its effect on the output z. The actuator is considered at the fixed position $(X_u, Y_u) = (100, 0)$

function. An approximate requirement for causality is that the time delay of the estimation be higher than that of the actuation. This establishes a maximum position for the input at $X_y \approx 84$ to result in a causal gain. This approximation corresponds closely to the observed trend for P parameter at $Y_y = -5$, as seen in Fig. 19: causality has a sharp increase as X_y is reduced from 90 to 80.

When the input sensor is in a position where a feedback scheme results, the behaviour of the gain becomes non-causal which in turn leads to a loss of efficiency of the actuation. This is illustrated in Fig. 21, comparing

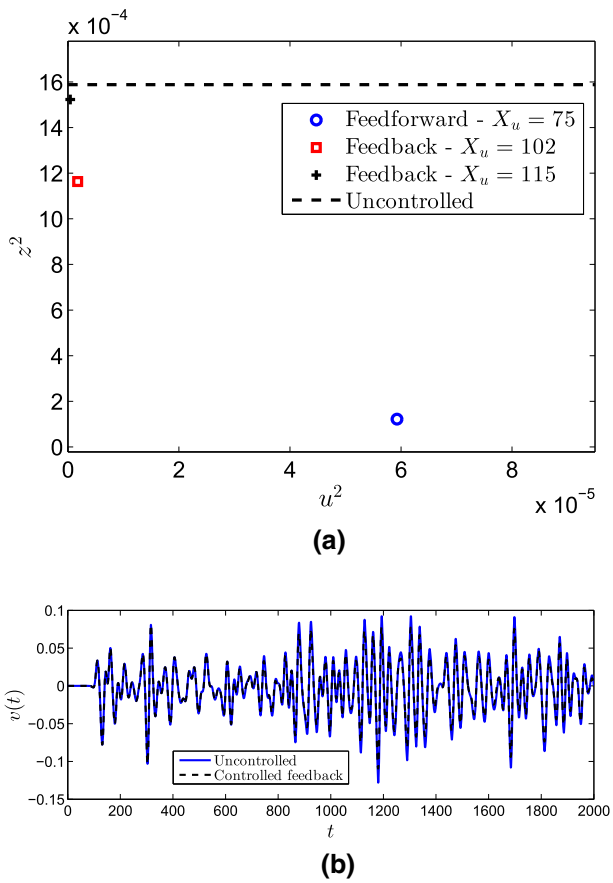

(a)

(b)

Fig. 21 Results for feedback control compared to corresponding feedforward configuration, actuation and objective are fixed at 100 and 125, respectively, input varies from 75 (feedforward configuration), 102 and 115 (feedback configurations). **a** MS values of the objective and actuation, **b** time series for a feedback configuration, for $X_u = 115$, in comparison with the open-loop behaviour

the RMS values of three feedback configurations. The resulting time signal of the output is also shown for one of the feedback setups.

The resulting causality of the gain justifies the use of feedforward configurations for flow control applications of convectively unstable flows, such as the present mixing layer, along with a minimum spacing between sensors and actuators such that a feedback path is not added to the scheme. Other output positions, closer to the actuation signal, were also tested in a feedback scheme and, although not shown, similar results were observed.

9 Conclusions

We have developed a framework for the closed-loop control of fluctuations, over a convectively unstable free shear flow, using PSE-based transfer functions. Both feedback and feedforward configurations were derived and differences understood in terms of the causality of the resulting convolution kernel for control, with feedforward control presenting more compelling results in terms of reduction of the objective.

These reduced-order models allow for an understanding of the mechanisms behind closed-loop control and permitted the determination of the most appropriate positions for actuation and sensing. This was made in terms of an evaluation of the causality, accuracy of reduced-order models in reproducing the nonlinear behaviour of the simulation and sensitivity to forcing. The advantage of the PSE TFs here, when compared to other strategies for model reduction, is that such estimates are made without the need to perform computationally expensive simulations for each configuration, allowing a rapid exploration of the parameters.

Reductions of more than one order of magnitude in the MS values of the objective fluctuation were observed at the output position, along with a delay in the vortex pairing and roll-up, which is desirable in aeroacoustic applications.

Implementation of these control laws for more complex flows, such as a turbulent jet, is yet to be demonstrated. Other than the more complex dynamics of such flows, experimental constraints, such as measurement noise and model uncertainties, constitute a more challenging task for the control laws, designed using a linearized framework. Some of these issues were replicated numerically in this work by means of Reynolds number variations, amplitude of inflow and unsensed perturbations, showing that depending of the case, the performance of the controller is not significantly degraded. Unsensed perturbations, introduced between input and output, yet present a difficult task for the feedforward controller considered. Recent works, such as Fabbiane et al. [17], deal with this matter by means of an adaptive scheme.

The control laws presented in this paper are a useful tool for the proof of concepts and replication of some of the experimental issues, and are therefore an important step to obtain this further goal.

Acknowledgements Kenzo Sasaki has received a scholarship from FAPESP, Grant Number 2016/25187-4. André V. G. Cavalieri and Peter Jordan have been supported by the Science Without Borders program, Project Number A073/2013. André V. G. Cavalieri was supported by a CNPq Grant 310523/2017-6.

Compliance with ethical standards

Conflict of interest: The authors declare that they have no conflict of interest.

Appendix 1: Parabolized stability equations

Consider the Reynolds decomposition of the physical variables $\boldsymbol{q}_\phi = \bar{\boldsymbol{q}} + \boldsymbol{q}'$ with $\bar{\boldsymbol{q}} = (U, V, P)^{\mathrm{T}}$ and $\boldsymbol{q}' = (u', v', p')^{\mathrm{T}}$, containing respectively the mean and the fluctuating part of the streamwise and transversal velocity and pressure. The linearized bidimensional incompressible Navier–Stokes equations in Cartesian coordinates are then written as:

$$\frac{\partial u'}{\partial t} + U\frac{\partial u'}{\partial X} + u'\frac{\partial U}{\partial X} + V\frac{\partial u'}{\partial Y} + v'\frac{\partial U}{\partial Y} = -\frac{\partial p'}{\partial X} + \frac{1}{Re}\left(\frac{\partial^2 u'}{\partial X^2} + \frac{\partial^2 u'}{\partial Y^2}\right) \tag{21a}$$

$$\frac{\partial v'}{\partial t} + U\frac{\partial v'}{\partial X} + u'\frac{\partial V}{\partial X} + V\frac{\partial v'}{\partial Y} + v'\frac{\partial V}{\partial Y} = -\frac{\partial p'}{\partial Y} + \frac{1}{Re}\left(\frac{\partial^2 v'}{\partial X^2} + \frac{\partial^2 v'}{\partial Y^2}\right) \tag{21b}$$

$$\frac{\partial u'}{\partial X} + \frac{\partial v'}{\partial Y} = 0. \tag{21c}$$

The parabolized stability equations are able to propagate in space a perturbation defined in the Fourier space. This requires the definition of an inflow perturbation, which is commonly taken as the solution of the problem defined in the locally parallel assumption and, for the case of sheared flows, the Kelvin–Helmholtz mode [36] is considered to dominate the dynamics of the flow.

Assuming a baseflow written as $\bar{\boldsymbol{q}} = (U(Y), 0, 0)^{\mathrm{T}}$ and a perturbation defined as a superimposition of normal modes due to the homogeneity in the streamwise direction

$$\boldsymbol{q}'_{\mathrm{LST}}(X, Y, t) = \int_\alpha \int_\omega \hat{\hat{\boldsymbol{q}}}(\alpha, Y, \omega) \mathrm{e}^{i(\alpha X - \omega t)} \mathrm{d}\alpha \mathrm{d}\omega. \tag{22}$$

where the double hat indicates a Fourier transform from x and t to α and ω. Introducing the *ansatz* (22) in (21) leads to the system

$$-i\omega\hat{\hat{u}} + i\alpha U\hat{\hat{u}} + \hat{\hat{v}}\frac{\partial U}{\partial Y} = -i\alpha\hat{\hat{p}} + \frac{1}{Re}\left(-\alpha^2\hat{\hat{u}} + \frac{\partial^2\hat{\hat{u}}}{\partial Y^2}\right) \tag{23a}$$

$$-i\omega\hat{\hat{v}} + i\alpha U\hat{\hat{v}} = -\frac{\partial\hat{\hat{p}}}{\partial Y} + \frac{1}{Re}\left(-\alpha^2\hat{\hat{v}} + \frac{\partial^2\hat{\hat{v}}}{\partial Y^2}\right) \tag{23b}$$

$$i\alpha\hat{\hat{u}} + \frac{\partial\hat{\hat{v}}}{\partial Y} = 0, \tag{23c}$$

where the explicit dependency on α and ω has been dropped to simplify the notation, which can be recast in the following matricial form,

$$\begin{pmatrix} -i\omega - \frac{1}{Re}\frac{\partial^2 \cdot}{\partial Y^2} & \frac{\partial U}{\partial Y} & 0 & 0 & 0 \\ 0 & -i\omega - \frac{1}{Re}\frac{\partial^2 \cdot}{\partial Y^2} & \frac{\partial \cdot}{\partial Y} & 0 & 0 \\ 0 & \frac{\partial \cdot}{\partial Y} & 0 & 0 & 0 \\ 0 & 0 & 0 & 1 & 0 \\ 0 & 0 & 0 & 0 & 1 \end{pmatrix} \begin{pmatrix} \hat{\hat{u}} \\ \hat{\hat{v}} \\ \hat{\hat{p}} \\ \alpha\hat{\hat{u}} \\ \alpha\hat{\hat{v}} \end{pmatrix} = \alpha \begin{pmatrix} -iU & 0 & -i & -\frac{1}{Re} & 0 \\ 0 & -iU & 0 & 0 & -\frac{1}{Re} \\ -i & 0 & 0 & 0 & 0 \\ 1 & 0 & 0 & 0 & 0 \\ 0 & 1 & 0 & 0 & 0 \end{pmatrix} \begin{pmatrix} \hat{\hat{u}} \\ \hat{\hat{v}} \\ \hat{\hat{p}} \\ \alpha\hat{\hat{u}} \\ \alpha\hat{\hat{v}} \end{pmatrix}. \tag{24}$$

leading to a generalized eigenvalue problem which the solution will be used as the first step in the PSE marching procedure.

The parabolized stability equations [21] allow instability wave evolution over a slowly varying baseflow to be modelled. The assumption of a slowly varying baseflow allows [13] us to decompose the perturbation associated with the frequency ω into slowly and rapidly varying wave-like parts [21],

$$\boldsymbol{q}'_{PSE}(X, Y, t) = \hat{\boldsymbol{q}}(X, Y, \omega)\, \mathrm{e}^{i\left(\int_0^X \alpha(\xi)\,\mathrm{d}\xi - \omega t\right)}. \tag{25}$$

$\hat{\boldsymbol{q}}(X, Y, \omega)$ is the slowly varying part and $\Gamma = \mathrm{e}^{i\left(\int_0^X \alpha(\xi)\,\mathrm{d}\xi - \omega t\right)}$ is the wave-like part. We introduce the decomposition (25) into (21). The first axial derivatives of α and the second axial derivatives of $\boldsymbol{q}$ are also not

considered, assuming a slow variation of these quantities, which leads to the parabolization of the equations. We obtain after simplifying by Γ

$$\begin{aligned}
&-i\omega\hat{u}+i\alpha U\hat{u}+U\frac{\partial\hat{u}}{\partial X}+\hat{u}\frac{\partial U}{\partial X}+\hat{v}\frac{\partial U}{\partial Y}+V\frac{\partial\hat{u}}{\partial Y}=-i\alpha\hat{p}-\frac{\partial\hat{p}}{\partial X}+\frac{1}{Re}\left(2i\alpha\frac{\partial\hat{u}}{\partial X}-\alpha^2\hat{u}+\frac{\partial^2\hat{u}}{\partial Y^2}\right)\\
&-i\omega\hat{v}+i\alpha U\hat{v}+U\frac{\partial\hat{v}}{\partial X}+\hat{u}\frac{\partial V}{\partial X}+\hat{v}\frac{\partial V}{\partial Y}+V\frac{\partial\hat{v}}{\partial Y}=-\frac{\partial\hat{p}}{\partial Y}+\frac{1}{Re}\left(2i\alpha\frac{\partial\hat{v}}{\partial X}-\alpha^2\hat{v}+\frac{\partial^2\hat{v}}{\partial Y^2}\right)\\
&\frac{\partial\hat{u}}{\partial X}+i\alpha\hat{u}+\frac{\partial\hat{v}}{\partial Y}=0.
\end{aligned}\tag{26}$$

where again the explicit dependence of the terms in X, Y and ω has been suppressed.
The system (26) can be written in matricial form, in accordance with [34]:

$$(E+\alpha F)\frac{\partial\hat{\boldsymbol{q}}}{\partial X}+(A+\alpha B+\alpha^2C)\hat{\boldsymbol{q}}=0,\tag{27}$$

with

$$\begin{aligned}
E&=\begin{pmatrix}U&0&1\\0&U&0\\1&0&0\end{pmatrix},\quad F=\begin{pmatrix}-\frac{2i}{Re}&0&0\\0&-\frac{2i}{Re}&0\\0&0&0\end{pmatrix},\\
A&=\begin{pmatrix}-i\omega+\frac{\partial U}{\partial X}+V\frac{\partial\cdot}{\partial Y}-\frac{1}{Re}\frac{\partial^2\cdot}{\partial Y^2}&\frac{\partial U}{\partial Y}&0\\\frac{\partial V}{\partial X}&-i\omega+\frac{\partial V}{\partial Y}+V\frac{\partial\cdot}{\partial Y}-\frac{1}{Re}\frac{\partial^2\cdot}{\partial Y^2}&\frac{\partial\cdot}{\partial Y}\\0&\frac{\partial\cdot}{\partial Y}&0\end{pmatrix},\\
B&=\begin{pmatrix}iU&0&i\\0&iU&0\\i&0&0\end{pmatrix},\quad C=\begin{pmatrix}\frac{1}{Re}&0&0\\0&\frac{1}{Re}&0\\0&0&0\end{pmatrix}.
\end{aligned}\tag{28}$$

Decomposition (25) is a priori not unique because of the presence of the x variable in $\hat{\boldsymbol{q}}(X,Y,\omega)$ as well in $\alpha(X)$ and because no evolution equation is given for α. In order to overcome this ambiguity, a normalization constraint is added [21] such that the exponential dependence (real and imaginary) is absorbed by the wave-like term $\mathrm{e}^{i\int_0^X\alpha(\xi)\,\mathrm{d}\xi}$:

$$\left(\hat{\boldsymbol{q}},\frac{\partial\hat{\boldsymbol{q}}}{\partial X}\right)_Y=\int_0^\infty\hat{\boldsymbol{q}}.\frac{\partial\hat{\boldsymbol{q}}}{\partial X}\,\mathrm{d}Y=0.\tag{29}$$

Starting with $(\hat{\boldsymbol{q}}_0,\alpha_0)$, $\hat{\boldsymbol{q}}(X,Y)$ may be obtained by integrating equation (27) in space using an implicit Euler scheme, with iterations (index (n)) in α such that the constraint (29) is respected [20]:

$$\begin{cases}\left(E+\alpha_{j+1}^{(n)}F+\Delta X\left(A+\alpha_{j+1}^{(n)}B+\left(\alpha_{j+1}^{(n)}\right)^2C\right)\right)_{j+1}\hat{\boldsymbol{q}}_{j+1}=\left(E_{j+1}+\alpha_{j+1}^{(n)}F\right)\hat{\boldsymbol{q}}_j\\ \alpha_{j+1}^{(n+1)}=\alpha_{j+1}^{(n)}-\dfrac{i}{\Delta X}\dfrac{\left(\hat{\boldsymbol{q}}_{j+1},\hat{\boldsymbol{q}}_{j+1}-\hat{\boldsymbol{q}}_j\right)_y}{\left(\hat{\boldsymbol{q}}_{j+1},\hat{\boldsymbol{q}}_{j+1}\right)_y}.\end{cases}\tag{30}$$

The iteration on α is based on the separation assumption (25) in conjunction with the normalization constraint $(\hat{\boldsymbol{q}},\frac{\partial\hat{\boldsymbol{q}}}{\partial X})_Y=0$.

Appendix 2: Kelvin–Helmholtz projection

To obtain the Kelvin–Helmholtz projection, the flow is considered locally parallel close to the perturbation so that one may write, for the two-dimensional case,

$$\mathcal{L}\begin{pmatrix}\hat{\hat{u}}(\alpha,Y,\omega)\\ \hat{\hat{v}}(\alpha,Y,\omega)\\ \hat{\hat{p}}(\alpha,Y,\omega)\\ \alpha\hat{\hat{u}}(\alpha,Y,\omega)\\ \alpha\hat{\hat{v}}(\alpha,Y,\omega)\end{pmatrix}-\alpha\mathcal{F}\begin{pmatrix}\hat{\hat{u}}(\alpha,Y,\omega)\\ \hat{v}(\alpha,y,\omega)\\ \hat{p}(\alpha,y,\omega)\\ \alpha\hat{\hat{u}}(\alpha,Y,\omega)\\ \alpha\hat{\hat{v}}(\alpha,Y,\omega)\end{pmatrix}=\begin{pmatrix}0\\ 0\\ 0\\ \hat{\hat{f}}_X(\alpha,Y,\omega)\\ \hat{\hat{f}}_Y(\alpha,Y,\omega)\end{pmatrix}, \tag{31}$$

where the variables and forcing terms are written in terms of their space and time Fourier transforms, $\hat{\hat{f}}$ denote the transform from X to α and from t to ω and the matrices $\mathcal{L}$ and $\mathcal{F}$ may be found in the "Appendix 1", on the definition of the locally parallel problem, Eq. 24.

$$\hat{\hat{f}}_X(\alpha,Y)=\int_{-\infty}^{\infty}f_X(X,Y)\mathrm{e}^{-i\alpha X}\mathrm{d}X \tag{32}$$

$$\hat{\hat{f}}_Y(\alpha,Y)=\int_{-\infty}^{\infty}f_Y(X,Y)\mathrm{e}^{-i\alpha X}\mathrm{d}X \tag{33}$$

Writing the velocity and pressure fluctuations as a linear combination of the eigenfunctions defined from the eigenvalue problem $\mathcal{L}\phi_i=\alpha_i\mathcal{F}\phi_i$, and defining the vectors $\hat{\hat{\boldsymbol{q}}}(\alpha,Y,\omega)=[\hat{\hat{u}},\,\hat{\hat{v}},\,\hat{\hat{p}},\,\alpha\hat{\hat{u}},\,\alpha\hat{\hat{v}}]^{\mathrm{T}}$ and $\hat{\hat{f}}(\alpha,Y,\omega)=[0,0,0,\,\hat{\hat{f}}_X,\,\hat{\hat{f}}_Y]^{\mathrm{T}}$

$$\hat{\hat{\boldsymbol{q}}}(\alpha,Y,\omega)=\sum_i^{\infty}a_i\hat{\hat{\phi}}_i(\alpha,Y,\omega), \tag{34}$$

Equation 31 becomes,

$$\sum_i^{\infty}\left[a_i\alpha_i F\hat{\hat{\phi}}_i(\alpha,Y,\omega)-a_i\alpha F\hat{\hat{\phi}}_i(\alpha,Y,\omega)\right]=\hat{\hat{f}}(\alpha,Y,\omega) \tag{35}$$

.

Performing the inner product with the adjoint problem $\hat{\hat{\psi}}_i(\alpha,Y,\omega)$, which result from the solution of

$$\mathcal{L}^{\dagger}\hat{\hat{\boldsymbol{q}}}(\alpha,Y,\omega)-\alpha\mathcal{F}^{\dagger}\hat{\hat{\boldsymbol{q}}}(\alpha,Y,\omega)=\hat{\hat{f}}(\alpha,Y,\omega), \tag{36}$$

where $L^{\dagger}$ and $F^{\dagger}$ indicate the conjugate transposes of matrices L and F.

$$\sum_i^{\infty}\left[a_i\alpha_i\langle\hat{\hat{\psi}}_j(\alpha,Y,\omega),F\hat{\hat{\phi}}_i(\alpha,Y,\omega)\rangle-a_i\alpha\langle\hat{\hat{\psi}}_j(\alpha,Y,\omega),F\hat{\hat{\phi}}_i(\alpha,Y,\omega)\rangle\right]=\langle\hat{\hat{\psi}}_j(\alpha,Y,\omega),\hat{\hat{f}}(\alpha,Y,\omega)\rangle. \tag{37}$$

Given that the eigenfunctions of the direct and adjoint problems are biorthogonal, i.e. $\langle\hat{\hat{\psi}}_j(\alpha,Y,\omega),F\hat{\hat{\phi}}_i(\alpha,Y,\omega)\rangle=\delta_{ij}$, Eq. (37) leads to,

$$a_j=\frac{\langle\hat{\hat{\psi}}_j(\alpha,Y,\omega),\hat{\hat{f}}(\alpha,Y,\omega)\rangle}{\alpha_j-\alpha} \tag{38}$$

Figure 22 presents the eigenspectrum for the mixing layer at the position of the actuator for two different discretizations, the different branches of the continuum spectrum corresponding to decaying modes along with the Kelvin–Helmholtz mode are clearly visible. Other stable modes, which have not yet converged, may also be observed.

We assume that the dynamics induced by the actuator will be dominated by the Kelvin–Helmholtz instability, the only unstable mode present in the problem, particularly as one moves further downstream of the actuator,

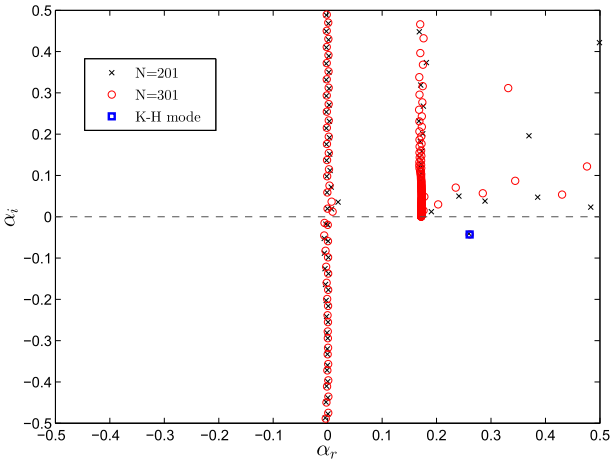

Fig. 22 Eigenspectrum for the mixing layer at the position of actuation

where transients caused by decaying modes are expected to have ceased. The flow fluctuations are thus given as

$$\hat{\hat{\boldsymbol{q}}}(\alpha, Y, \omega) = \sum_j \frac{\langle \hat{\hat{\psi}}_j(\alpha, Y, \omega), \hat{\hat{f}}(\alpha, Y, \omega) \rangle}{\alpha_j - \alpha} \hat{\hat{\phi}}_j(\alpha, Y, \omega) \approx \frac{\langle \hat{\hat{\psi}}_{\mathrm{KH}}(\alpha, Y, \omega), \hat{\hat{f}}(\alpha, Y, \omega) \rangle}{\alpha_{\mathrm{KH}} - \alpha} \hat{\hat{\phi}}_{\mathrm{KH}}(\alpha, Y, \omega) \quad (39)$$

where $\hat{\hat{\phi}}_{\mathrm{KH}}(\alpha, Y, \omega)$ and α_{KH} are respectively eigenfunction and eigenvalue corresponding to the Kelvin–Helmholtz mode. The inverse Fourier transform of Eq. (39) gives the fluctuation in the (X, Y) domain as

$$\hat{\boldsymbol{q}}(X, Y, \omega) = \frac{1}{2\pi} \int_{-\infty}^{\infty} \frac{\langle \hat{\hat{\psi}}_{\mathrm{KH}}(\alpha, Y, \omega), \hat{\hat{f}}(\alpha, Y, \omega) \rangle}{\alpha_{\mathrm{KH}} - \alpha} \hat{\hat{\phi}}_{\mathrm{KH}}(\alpha, Y, \omega) \mathrm{e}^{i\alpha X} \mathrm{d}\alpha. \quad (40)$$

Integration of equation 40 is made in the complex plane and consists of a contour path idented below the Kelvin–Helmholtz mode to satisfy causality [26]. For X downstream of the actuation position X_u, this integral can be evaluated using the residue theorem by closing the integration contour with a semi-circle in the upper half plane, since the integrand will vanish for $\Im(\alpha) > 0$. The integral will be equal to the residue calculated at α_{KH}, plus contributions from residues of other stable modes and from the continuous branches of the spectrum [2]. Sufficiently downstream of the forcing one expects the Kelvin–Helmholtz contribution to dominate, as it is the sole unstable mode. The velocity fluctuations become, for a given force $f(X, Y, t)$ as given as,

$$\hat{\boldsymbol{q}}(X, Y, \omega) = i \langle \hat{\hat{\Psi}}_{\mathrm{KH}}(\alpha_{\mathrm{KH}}, Y, \omega), \hat{\hat{f}}(\alpha_{\mathrm{KH}}, Y, \omega) \rangle \mathrm{e}^{i\alpha_{\mathrm{KH}} X} \hat{\hat{\phi}}_{\mathrm{KH}}(\alpha_{\mathrm{KH}}, Y, \omega) \quad (41)$$

which is then used as the first step for the PSE marching method.

References

1. Akers, J.C., Bernstein, D.S.: Armarkov least-squares identification. In: American Control Conference, 1997. Proceedings of the 1997, vol. 1, pp. 186–190. IEEE (1997)
2. Ashpis, D.E., Reshotko, E.: The vibrating ribbon problem revisited. J. Fluid Mech. **213**, 531–547 (1990)
3. Bagheri, S., Henningson, D.S., Hoepffner, J., Schmid, P.J.: Input-output analysis and control design applied to a linear model of spatially developing flows. Appl. Mech. Rev. **62**(2), 020,803 (2009)
4. Belson, B.A., Semeraro, O., Rowley, C.W., Henningson, D.S.: Feedback control of instabilities in the two-dimensional blasius boundary layer: the role of sensors and actuators. Phys. Fluids (1994-present) **25**(5), 054,106 (2013)
5. Bendat, J.S., Piersol, A.G.: Random Data: Analysis and Measurement Procedures, vol. 729. Wiley, New York (2011)
6. Biau, D.: Transient growth of perturbations in stokes oscillatory flows. J. Fluid Mech. **794**, R4 (2016)
7. Biringen, S.: Active control of transition by periodic suction-blowing. Phys. Fluids (1958–1988) **27**(6), 1345–1347 (1984)
8. Bridges, J., Brown, C.A.: Parametric testing of chevrons on single flow hot jets. AIAA Paper **2824**, 2004 (2004)
9. Cavalieri, A.V.G., Jordan, P., Gervais, Y., Wei, M., Freund, J.B.: Intermittent sound generation and its control in a free-shear flow. Phys. Fluids **22**, 115113 (2010)

10. Chen, K.K., Rowley, C.W.: H 2 optimal actuator and sensor placement in the linearised complex Ginzburg–Landau system. J. Fluid Mech. **681**, 241–260 (2011)
11. Cheung, L.C., Lele, S.K.: Linear and nonlinear processes in two-dimensional mixing layer dynamics and sound radiation. J. Fluid Mech. **625**, 321–351 (2009)
12. Colonius, T., Lele, S.K., Moin, P.: Sound generation in a mixing layer. J. Fluid Mech. **330**, 375–409 (1997)
13. Crighton, D.G., Gaster, M.: Stability of slowly diverging jet flow. J. Fluid Mech. **77**(2), 387–413 (1976)
14. Devasia, S.: Should model-based inverse inputs be used as feedforward under plant uncertainty? IEEE Trans. Autom. Control **47**(11), 1865–1871 (2002)
15. Devasia, S., Chen, D., Paden, B.: Nonlinear inversion-based output tracking. IEEE Trans. Autom. Control **41**(7), 930–942 (1996)
16. Fabbiane, N., Bagheri, S., Henningson, D.S.: Energy efficiency and performance limitations of linear adaptive control for transition delay. J. Fluid Mech. **810**, 60–81 (2017)
17. Fabbiane, N., Semeraro, O., Bagheri, S., Henningson, D.S.: Adaptive and model-based control theory applied to convectively unstable flows. Appl. Mech. Rev. **66**(6), 060,801 (2014)
18. Fabbiane, N., Simon, B., Fischer, F., Grundmann, S., Bagheri, S., Henningson, D.S.: On the role of adaptivity for robust laminar flow control. J. Fluid Mech. **767**, R1 (2015)
19. Gautier, N., Aider, J.L.: Feed-forward control of a perturbed backward-facing step flow. J. Fluid Mech. **759**, 181–196 (2014)
20. Gudmundsson, K., Colonius, T.: Instability wave models for the near-field fluctuations of turbulent jets. J. Fluid Mech. **689**, 97–128 (2011)
21. Herbert, T.: Parabolized stability equations. Annu. Rev. Fluid Mech. **29**(1), 245–283 (1997)
22. Hervé, A., Sipp, D., Schmid, P.J., Samuelides, M.: A physics-based approach to flow control using system identification. J. Fluid Mech. **702**, 26–58 (2012)
23. Hill, D.C.: Adjoint systems and their role in the receptivity problem for boundary layers. J. Fluid Mech. **292**, 183–204 (1995)
24. Huerre, P., Batchelor, G.K., Moffatt, H.K., Worster, M.G.: Open shear flow instabilities. In: Perspectives in fluid dynamics - A collective introduction to current research. Cambridge University Press, pp. 159–229 (2000)
25. Huerre, P., Monkewitz, P.A.: Absolute and convective instabilities in free shear layers. J. Fluid Mech. **159**, 151–168 (1985)
26. Huerre, P., Monkewitz, P.A.: Local and global instabilities in spatially developing flows. Annu. Rev. Fluid Mech. **22**(1), 473–537 (1990)
27. Juang, J.N., Pappa, R.S.: An eigensystem realization algorithm for modal parameter identification and model reduction. J. Guid. **8**(5), 620–627 (1985)
28. Kachanov, Y.S.: Physical mechanisms of laminar-boundary-layer transition. Annu. Rev. Fluid Mech. **26**(1), 411–482 (1994)
29. Kim, J., Bewley, T.R.: A linear systems approach to flow control. Annu. Rev. Fluid Mech. **39**, 383–417 (2007)
30. Koenig, M., Sasaki, K., Cavalieri, A.V.G., Jordan, P., Gervais, Y.: Jet-noise control by fluidic injection from a rotating plug: linear and nonlinear sound-source mechanisms. J. Fluid Mech. **788**, 358–380 (2016)
31. Lajús, F.C., Deschamps, C.J., Cavalieri, A.V.G.: Spatial stability characteristics of non-circular jets. In: 21st AIAA/CEAS Aeroacoustics Conference, p. 2537 (2015)
32. Le Rallic M., Jordan, P., Gervais, Y.: Jet-noise reduction: the effect of azimuthal actuation modes. In: 22nd AIAA/CEAS Aeroacoustics Conference, p. 2868 (2016)
33. Levin, O., Henningson, D.S.: Exponential vs algebraic growth and transition prediction in boundary layer flow. Flow Turbul. Combust. **70**(1–4), 183–210 (2003)
34. Li, F., Malik, M.R.: On the nature of pse approximation. Theor. Comput. Fluid Dyn. **8**(4), 253–273 (1996)
35. Li, Y., Gaster, M.: Active control of boundary-layer instabilities. J. Fluid Mech. **550**, 185–205 (2006)
36. Michalke, A.: Survey on jet instability theory. Prog. Aerosp. Sci. **21**, 159–199 (1984)
37. Mitchell, B.E., Lele, S.K., Moin, P.: Direct computation of the sound generated by vortex pairing in an axisymmetric jet. J. Fluid Mech. **383**, 113–142 (1999)
38. Ogata, K., Yang, Y.: Modern Control Engineering, vol. 4. Prentice hall (2002)
39. Press, W.H.: Numerical Recipes 3rd Edition: The Art of Scientific Computing. Cambridge University Press, Cambridge (2007)
40. Sasaki, K., Piantanida, S., Cavalieri, A.V., Jordan, P.: Real-time modelling of wavepackets in turbulent jets. J. Fluid Mech. **821**, 458–481 (2017)
41. Schmid, P.J., Sipp, D.: Linear control of oscillator and amplifier flows. Phys. Rev. Fluids **1**(4), 040,501 (2016)
42. Semeraro, O., Pralits, J.O., Rowley, C.W., Henningson, D.S.: Riccati-less approach for optimal control and estimation: an application to two-dimensional boundary layers. J. Fluid Mech. **731**, 394–417 (2013)
43. Sinha, A., Gaitonde, D.V., Sohoni, N.: Parabolized stability analysis of dual-stream jets. In: 22nd AIAA/CEAS Aeroacoustics Conference, p. 3057 (2016)
44. Sipp, D., Schmid, P.: Closed-loop control of fluid flow: a review of linear approaches and tools for the stabilization of transitional flows. AerospaceLab **2013**(6), 1–11 (2013)
45. Thomas, A., Saric, W.: Harmonic and subharmonic waves during boundary-layer transition. Bull. Am. Phys. Soc. **26**, 1252 (1981)
46. Thomas, A.S.: The control of boundary-layer transition using a wave-superposition principle. J. Fluid Mech. **137**, 233–250 (1983)
47. Violato, D., Scarano, F.: Three-dimensional vortex analysis and aeroacoustic source characterization of jet core breakdown. Phys. Fluids (1994-present) **25**(1), 015,112 (2013)
48. Wei, M., Freund, J.: A noise controlled free shear flow. J. Fluid Mech. **546**, 123–152 (2006)
49. White, E.B., Saric, W.S.: Application of variable leading-edge roughness for transition control on swept wings. AIAA Paper **283**, 2000 (2000)